Mapping the ionised gas in active galactic nuclei with spectral-timing and spectroscopy

Juráňová, A.

Publication date
2024

Chapter 3

Bridging the gaps: Prospects for probing AGN outflows with Fourier timing

A. Juráňová, P. Uttley, and E. Costantini

In preparation.

Abstract

Ionised absorbers are commonly observed in AGN X-ray spectra. Depending on the properties of the incident radiation and the gas density and average ionisation, the outflows can show complex, frequency-dependent variability. Expanding our earlier investigation of the spectral-timing behaviour of ionised outflows in a highly variable AGN, we aim to probe a different, highly coherent, regime of the absorber response relative to the system presented in Juráňová et al. (2022). We simulate the response of photoionised gas to changes in the ionising flux for a wide range of gas conditions and perform Fourier spectral-timing analysis of an AGN–outflow system similar to that in MCG–06-30-15. Additionally, we examine the sensitivity of our modelling to observational uncertainties associated with the variability of the emission source. Our analysis reveals that the unknown history of the system does not significantly impact the absorber timing properties recovered from the observed periods. The continuum variability properties together with the moderate column density and turbulent line broadening of the simulated warm absorbers result in nearly unity intrinsic coherence of all absorption-affected energy bands. Hence, the Fourier time lags are reliably measurable and can exceed $\sim$100 s below 10^{-4} Hz, but diminish with increasing frequency. Finally, we show that the power spectral density of absorption-affected spectral bands can be used to identify and characterise the absorber variability, potentially enabling constraints on the density and distance of ionised outflows from currently available data.

3.1 Introduction

Outflows of ionised gas are common constituents of active galactic nuclei (AGNs). Those observable via absorption in the X-ray band have been detected in more than 50% of nearby, X-ray-bright AGN (e.g. Tombesi et al. 2013; Laha et al. 2014). While believed to play a crucial role in connecting the central engine and the large-scale effects observed in the host galaxy environment (Ferrarese & Merritt 2000), a lot remains to be understood about their origin, structure and even their location in the system (see e.g. Giustini & Proga 2019; Laha et al. 2021, for a review).

The outflow absorption spectra consist primarily of strong lines of highly abundant elements, such as Fe, C, N, O, Ne, Si, S, or Mg, with the ionic composition tightly connected to the spectral distribution of the central X-ray–UV radiation field. When in photoionisation equilibrium, the ionisation state of the gas can be globally characterised by the ratio of the ionising flux to the gas-particle density n, referred to as the ionisation parameter $\xi = L_{\rm ion}/(nr^2)$, where the ionising luminosity $L_{\rm ion}$ is the luminosity in the energy range $1-1000$ Ryd and r stands for the distance to the ionising source (Kallman & Bautista 2001).

The AGN emission can be, however, substantially variable. Whether equilibrium can be reached then depends on the rate at which the gas ionisation can change, relative to the flux variability timescale (Krolik & Kriss 1995b). As a result, the relation between the changes in the incident ionising photon flux and the absorbing medium can be rather complex (Nicastro et al. 1999b). The nature of the response is given by the recombination timescale, explicitly dependent on the gas density, which has been recently quantitatively demonstrated by Rogantini et al. (2022) for a wide range of gas conditions. In practice, the ionic concentrations can follow three qualitatively different scenarios. When the density is sufficiently high, resulting in an effectively instantaneous response, equilibrium is reached with the immediate incident radiation field. When, in contrast, the recombination timescale exceeds the variability timescale, the changes in the ionic concentrations are delayed and smoothed relative to the ionising flux. With even longer recombination time, these effects further increase until a steady equilibrium is reached. With the growing number of longer and deeper observations, the prospects of identifying these time-dependent effects increase. Following this trend, complex models of the non-equilibrium spectra have recently been explored (Rogantini et al. 2022; Luminari et al. 2023; Sadaula & Kallman 2024).

As the gas density cannot be directly determined from X-ray spectra (see, however, Kaastra et al. 2004), measuring the time-dependent effects resulting from the recombination timescale presents a promising way to constrain this elusive gas property. The evolution of ionic concentrations can be studied in the time domain, by measuring the delayed ionisation state (e.g. Kaastra et al. 2012; Rogantini et al. 2022) or the broadened distribution of ionic species present in the time-averaged spectrum (Gu et al. 2023). Another approach involves the use of the general properties of the timescale-resolved variability, accessible with Fourier spectral-timing methods (e.g. Uttley et al. 2014).

As first shown by Silva et al. (2016), the delay in the absorption response results in Fourier-frequency- and flux-dependent time lags, which can in principle be measured in the data. Unambiguous measurements of absorption-related time lags require, however, high resolution of the analysed lag-energy spectra to isolate the absorbers from other lagging components (e.g. the reflection spectrum, Fabian et al. 2009; Zoghbi et al. 2012). On the other hand, time lags are not the only aspects of variable absorption detectable with Fourier spectral-timing. The absorber response is, in principle, non-linear, and thus to some extent intrinsically incoherent. Provided the incoherent signal is sufficiently strong, this aspect of absorption variability is also measurable with spectral-timing analysis (first reported by Silva et al. 2016), and could be used to recover the gas properties. This approach has been applied to observations of variable obscuration by high-column-density gas in NGC 3783 by De Marco et al. (2020), and, as shown in Juráňová et al. (2022), is expected to be applicable also to somewhat less extreme absorption associated with ultra-fast outflows (UFOs; e.g. Tombesi et al. 2010; Cappi et al. 2013b). It should be noted, however, that the observable Fourier spectral-timing properties of the absorption-modulated data are impacted by the properties of the underlying emission signal, which translate into the strength and variability of different absorption lines in the time-dependent spectra.

Since the absorber variability amplitude scales with that of the continuum, stronger features are generally produced at longer timescales (Silva et al. 2016; Juráňová et al. 2022). Therefore, long observing campaigns are particularly suitable to target those effects. However, the long gaps separating individual observations limit the knowledge of the behaviour of the ionising continuum, needed to correctly predict the time-dependent ionic concentrations throughout the campaign. In recent years, employing Gaussian processes (GP) has proven successful in modelling the stochastic AGN variability (e.g. Kelly et al. 2014). This approach has proven reliable in the recovery of several key properties of AGN variability, including the autocorrelation functions and time lags (Wilkins 2019; Griffiths et al. 2021; Lewin et al. 2022). Bridging the gaps between observations with realistic GP-generated light curves can provide insight into the impact of unobserved changes in ionising radiation.

While absorption-related effects are occasionally alluded to in timing studies focused on the relation between the X-ray emission components, the understanding of their Fourier spectral-timing properties is incomplete. Our previous work, dedicated to capabilities of the future X-ray observatory *Athena* for the spectral-timing analysis of time-dependent AGN outflows (Juráňová et al. 2022), addresses the case of an extremely variable source. Additionally, the column density of the modelled outflows is relatively high and the assumed line broadening (1000 $\mathrm{km\,s^{-1}}$), chosen to represent properties in UFOs, effectively increases the extent of variations in the transmission spectrum by suppressing saturation effects. Here, we investigate the spectral-timing properties of the slower ($v_{\rm out} \sim 10^2 - 10^3\ \mathrm{km\,s^{-1}}$), typically less ionised counterparts of UFOs, termed warm absorbers (WAs; e.g. Reynolds & Fabian 1995; Tombesi et al. 2013; Laha et al. 2014).

This paper is structured as follows. In Sect. 3.2, we describe the properties of the simulated radiation source and the absorbing ionised outflows and present the methodology used to derive synthetic observations of the time-variable system. The Fourier timing properties derived from the simulated data are presented in Sect. 3.3, with special attention to the impact of uncertainties in the underlying source variability. The discussion in Sect. 3.4

establishes our expectations for the signatures of variable WAs in the presently available data. Our findings are summarised in Sect. 3.5.

3.2 Simulation setup

The simulations are based on the *XMM-Newton* observing campaign of MCG–06-30-15 performed in 2001. The data consist of three observations, approximately 89, 129, and 130 ks long, separated by gaps of $\sim$50 ks. During this campaign, the spectral shape of the X-ray continuum was remarkably stable, changing only in the overall normalisation. The observations capture variations of the continuum flux typically of a factor of two on kilo-second timescales, but on longer timescales, the observed flux changes by a factor of four. The continuum source is rather bright, with the mean flux in the nearly unabsorbed 2–10 keV band being approximately 5×10^{-11} erg s^{-1} cm^{-2}.

3.2.1 Incident ionising SED

The shape of the incident ionising spectral energy distribution (SED) is reconstructed based on the MCG–06-30-15 average spectrum extracted from the first and the third observation of the campaign (with observation IDs 0029740101 and 0029740801), identical in both spectral shape and the total flux. The data were processed with the *XMM-Newton* Science Analysis System v20.0.0, following the standard procedures, and the spectrum was analysed in the fitting package SPEX v3.07.03 (Kaastra et al. 1996; Kaastra et al. 2023). We note that while we aim to reconstruct a realistic continuum spectrum of this source, we maintain a phenomenological approach and we do not discuss the physical implications of the continuum components.

For the low-energy part of the ionising spectrum, we analysed the photometric measurements from the Optical Monitor, available in the *U* filter. To correct for the contamination by the stellar emission from the host galaxy, we scaled the extracted flux by a factor of 0.15, following the approach of Arévalo et al. (2005). The AGN emission in the UV band is in our modelling represented by a disc black-body component (`dbb` in SPEX), with the electron temperature fixed to 10 eV. As shown for example in Vasudevan & Fabian (2009), this source is strongly affected by intrinsic dust extinction. Assuming the ionised absorbers are located closer in relative to the dust, we corrected for the reddening, using $E(B-V) = 0.6$ and the Gordon et al. (2003) Small Magellanic Cloud Bar Average extinction law with $R_V = 2.74$.

To construct the spectrum of the X-ray continuum, we used the following approach. Assuming this disc emission provides the seed photons for Comptonisation in the warm corona (Done et al. 2012; Kubota & Done 2018), we used the corresponding model `comt` for the description of the X-ray soft excess. The observed spectrum was well-reconstructed with the optical depth $\tau \approx 52$ and the electron temperature equivalent to $kT \approx 0.15$ keV, where k is the Boltzmann constant. The primary power-law continuum is described by the index $\Gamma \approx 2.15$ and it is cut off exponentially at 150 keV (Guainazzi et al. 1999). Finally, the model is completed with a reflection component (`refl` in SPEX; Magdziarz & Zdziarski 1995; Zycki et al. 1999) that

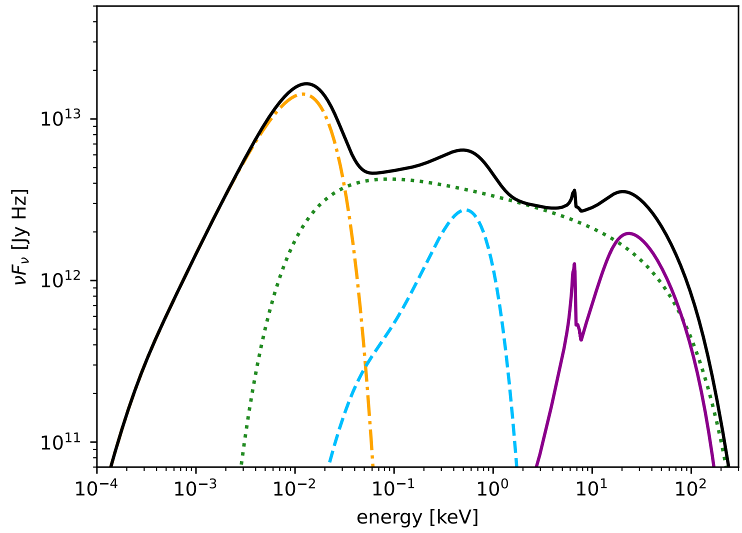

Figure 3.1: Average incident ionising SED. The individual components of the complete SED (solid black line) are given as follows. The disc black body is displayed as the dashed-dotted orange curve, the power-law exponentially cut-off at both ends is shown as a dotted green curve, the Comptonisation component with a dashed blue line and the reflection component with a solid purple line.

gives rise to the observed iron Kα line and an enhancement in the hard X-ray continuum (see e.g. Brenneman & Reynolds 2006). The complete SED and the individual components are visualised in Fig. 3.1.

3.2.2 Ionised absorbers

The X-ray spectrum of MCG–06-30-15 has a complex absorption spectrum formed by features from dust and warm absorbers (e.g. Lee et al. 2002; Turner et al. 2003; Young et al. 2005; Chiang & Fabian 2011). In the simulations, we assume the ionised absorbing medium to be represented by three WAs, each with a unity covering fraction, that provide a good fit of the EPIC-pn spectrum. For the fitting, we fixed the velocity shifts of the absorbers to the values constrained by Laha et al. (2014), who performed spectral fitting of the 0029740701 RGS observation (Table 3.1). The metallicity of the gas is assumed to be Solar, with elemental abundances of Lodders et al. (2009). The transmission of these absorbers throughout the simulation is depicted in Fig. 3.2.

The ionisation parameter of the low-ionisation absorber is $\log\xi = 0.95$, where ξ is in units of erg s^{-1} cm and its hydrogen column density is $N_{\mathrm{H}} = 4.11 \times 10^{21}$ cm^{-2}. As can be seen in Fig. 3.2, this component has the strongest effect on the spectrum, absorbing as much as 50% of the underlying continuum. The strongest absorption occurs in the iron unresolved transition array (UTA; Behar et al. 2001) around 0.75 keV, formed by iron M-shell transitions. The

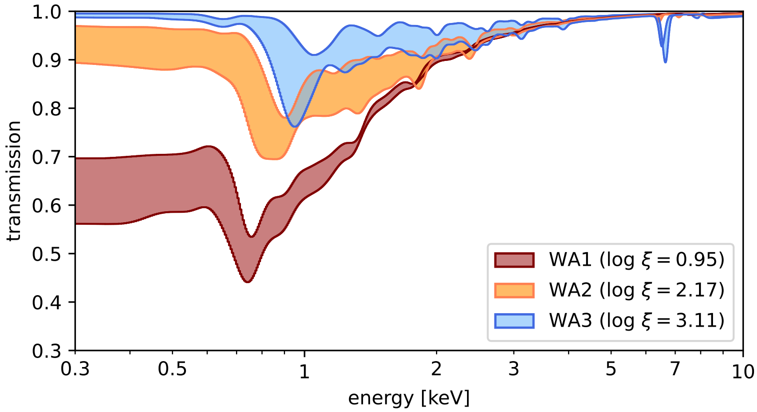

Figure 3.2: Transmission spectra of the three simulated ionised absorbers. The contours show the transmission of each absorber in the minimum and maximum ionisation reached during the time-evolving-gas simulation. The transmission spectra are given assuming the energy resolution of EPIC-pn.

Table 3.1: Global properties of the simulated warm absorbers based on EPIC-pn spectral fitting.

absorber	$\log \xi$	$N_{\rm H}$ [10^{21} cm^{-2}]	v [km s^{-1}]
WA1	0.95	4.11	−870
WA2	2.17	6.13	−450
WA3	3.11	13.6	−2370

Notes. The outflow velocities v are taken from Laha et al. (2014).

second WA has $\log \xi = 2.2$, with a significant contribution also from L-shell iron transitions around 1 keV. The ionisation of the last component is considerably higher, $\log \xi = 3.1$, with prominent absorption between 6–7 keV from Fe K-shell lines. Taking advantage of these distinct numerical values of the ionisation parameter, we later refer to these outflows as WA1, WA2, and WA3, in the order of increasing ionisation. The global spectral properties of the WAs are summarised in Table 3.1.

The ionisation parameter together with the ionising luminosity provides the relation between the gas density and its distance to the ionising source (see Sect. 3.1). As the distance can be a more intuitive characteristic, aiding in relating the outflows to other physical components of the AGN environment, we adopt it as the defining quantity to distinguish outflows with a different recombination timescale throughout the paper. For reference, we note that the distance of $r = 10^{17}$ cm corresponds approximately to the hydrogen number density of 6×10^8 cm^{-3} for WA1, 4×10^7 cm^{-3} for WA2, and 4×10^6 cm^{-3} in the case of WA3.

3.2.3 Ionising source variability

To recreate realistic conditions for the changing incident ionising radiation, we define the SED variability in the following way. As the MCG–06-30-15 spectrum is only marginally affected by the WAs above 3 keV, we take the light curves recorded in the 3–10 keV range of EPIC-pn observations as representative of the continuum variations. Consistently with the observed spectra, we let the SED components dominant in the X-ray band vary by the same factor, resulting in a constant spectral shape of the underlying emission. As the timing properties of the absorbers are not significantly influenced by typical continuum lags (Juráňová et al. 2022), we do not take into account this behaviour and assume synchronous changes of all X-ray emission components. Furthermore, the UV continuum varies with a considerably smaller amplitude relative to the X-ray variability (Arévalo et al. 2005), so the disc emission is kept fixed in the simulation for simplicity. These choices allow us to examine the absorber timing behaviour in realistic conditions isolated from unrelated background effects.

3

Depending on the recombination timescale, the absorption properties may reflect the time-dependent behaviour of incident radiation happening well before the start of each observation. This fact thus intrinsically limits the accuracy of the predicted gas behaviour. Moreover, additional gaps may arise in the data due to periods of high background. To explore and quantify the effects introduced by the unknown variability history of the system, we use a set of light curves consistent with our data, assuming a stationary underlying variability process.

We modelled the AGN stochastic variability as a Gaussian process (Rasmussen & Williams 2006), with a continuous-time autoregressive moving average (CARMA) model (Kelly et al. 2009), using its simplest form, CAR(1), which represents the variability as a damped random walk (DRW). With this model, the power-spectral density (see Uttley et al. 2014) is described as a Lorentzian centred at zero frequency, leaving only two free parameters to be determined in the fitting process: the width of the Lorentzian (the bending frequency of the power spectrum) and the overall normalisation. Using this model, the low- and high-frequency slopes of the power-law distribution are fixed to 0 and -2, respectively, which somewhat simplifies the power-spectrum profile reported for MCG–06-30-15 by McHardy et al. (2005). Nevertheless, this approach is suitable for our purposes, as we aim to examine the effects associated with the general observational limitations rather than directly compare these simulations to data.

We found the maximum likelihood estimate of the DRW model parameters given the observed light curve using EzTao (Yu & Richards 2022), a Python package based on the library celerite (Foreman-Mackey et al. 2017). This library provides tools for fitting Gaussian processes, as well as tools for simulating datasets from a given CARMA model with a conditional distribution, thus reflecting constraints from the observed data. As the input, we used the above-described light curve extracted from all three observations, sampled with 200 s time steps. Aiming to generate synthetic light curves that reflect the uncertainty of the DRW fit, we used Markov-Chain Monte Carlo to sample the parameter distribution. Drawing 20 samples – constrained to match the data – of the DRW model, we generated synthetic light curves starting 100 ks before the initial observation and ending with the last, totalling

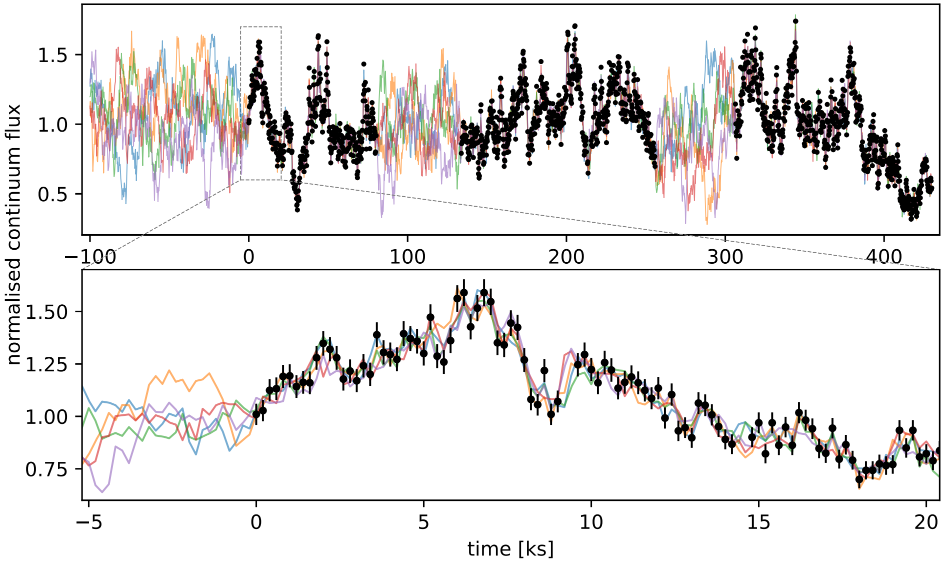

Figure 3.3: Generated continuum light curves and the measured normalised 3–10 keV continuum flux of MCG–06-30-15. Five samples (coloured lines) of the simulated variability consistent with the observed data points (black) are plotted for the entire simulation (top panel) and a small portion of the light curve around the beginning of the first observation ($t = 0$ ks; bottom panel).

530 ks per sample. An example of five of these light curves overlaid with the measured data points is given in Fig. 3.3.

3.2.4 Synthetic observations

To simulate the evolution of the absorption spectrum of each outflow, the ionic concentrations, given in our parametrisation only by the incident ionising radiation and the gas density and average ionisation, need to be obtained. Assuming for simplicity that the outflows can be modelled as a homogeneous slab of photoionised gas, we first obtain the photoionisation equilibrium rates with Cloudy (Ferland et al. 2017). To ensure numerical stability in the subsequent step, we calculated the photoionisation and recombination rates for each of the twenty light curves with a smaller time step, namely 20 s, linearly interpolating from the input data (with 200 s step).

Following the steps detailed in Juráňová et al. (2022), we assume the evolution of the time-dependent ionic concentrations can be described with a set of ionisation balance equations as defined in eq. (2) in Juráňová et al. (2022), first presented in Krolik & Kriss (1995b). For each absorber, we solved these differential equations independently assuming a clear view of the ionising continuum, aiming to later investigate the timing properties in isolation from contaminating effects from other components. For the first step of the integration, we considered the initial conditions to be described by the equilibrium concentrations.

Working with a sample of twenty light curves with generally different initial conditions, we note that the equilibrium ionisation was appropriately scaled so that the observed segments were described with an identical mean ionisation parameter in each simulation run. The time-dependent concentrations were calculated for a grid of densities, corresponding to distances in the range of $10^{16} - 10^{20}$ cm for each of the three outflows. This radial range covers the full extent of the possible outflow variability on the probed timescales, ranging from effectively instantaneous response to the ionising flux to a steady-state equilibrium set by the time-averaged radiation field.

Synthetic observations of the emission source absorbed by the simulated time-dependent outflows were generated with SPEX, using the continuum model as described in Sect. 3.2.1. The ionised absorption was modelled with the `slab` component. To simulate realistic photon fluxes, reduced by the environment along the line of sight, we included also foreground Galactic absorption by neutral gas with hydrogen column density of 4.74×10^{20} cm^{-2} (Willingale et al. 2013) and the dust in the AGN (see Lee et al. 2001; Turner et al. 2003), and redshifted the source spectrum to $z = 0.00775$ (Fisher et al. 1995), corresponding to the MCG–06-30-15 distance.

To probe the prospects of detecting spectral-timing signatures of variable absorption with currently available instruments, we generated the synthetic time-dependent spectra assuming the instrumental-response of EPIC-pn. Additionally, to verify whether our findings about the absorber behaviour are intrinsic to the simulated system or result rather from the limitations induced by the instrument capabilities, we used also the response representing the anticipated properties of the future *Athena X-ray observatory* (Nandra et al. 2013), specifically the onboard X-ray Integral Field Unit (X-IFU; Barret et al. 2018). We note that while this instrument will have inherently different lengths of the maximal continuous exposure as well as of the gaps between observations, we assume the same conditions as examined above for simplicity. Finally, we remind that the parts of the simulations that correspond to the *XMM-Newton* observation gaps were not considered in the analysis.

3.3 Spectral-timing properties

The results presented below were obtained with the methodology presented in Uttley et al. (2014). The analysis was conducted averaging over eight segments of the simulated data based on the original observations with *XMM-Newton* (Sect. 3.2), using a 200 s time step and a segment length of 40 ks, thus covering temporal frequencies ranging from 2.5×10^{-5} to 2.5×10^{-3} Hz. We note that three of the eight segments were directly preceded by observation gaps, where the continuum light curves for each simulation run differ considerably (see Fig. 3.3).

The timing properties were computed for bands of interest defined in the 0.3−7 keV range, where the spectrum was divided into 50 (for simulations with the resolution of EPIC-pn) or 100 (for X-IFU) contiguous bands, equally spaced on a logarithmic scale. For the reference light curves, we used the 7–10 keV band. This selection was made for two reasons: the reference band should be ideally completely free of contamination from the outflows, and,

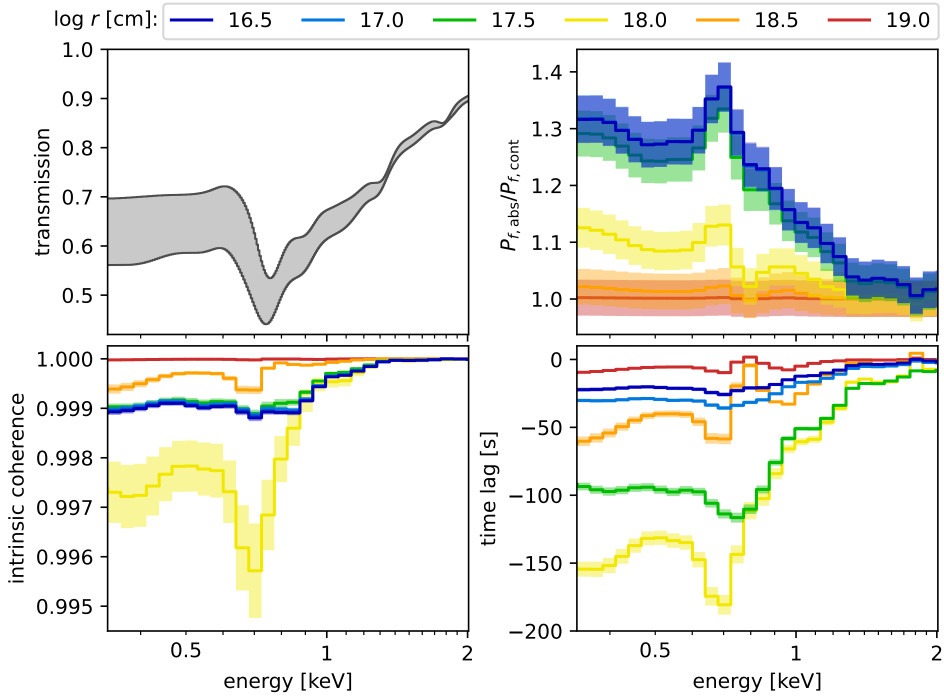

Figure 3.4: Fourier spectral-timing properties of the low-ionisation WA ($\log\xi = 0.95$) averaged over the frequency bin of $(3.75-7.5)\times10^{-5}$ Hz. In the upper-left panel, the transmission spectrum is given for reference. The power spectral density normalised by that of the unabsorbed continuum, intrinsic coherence, and time lags are given for absorbers at six radii. Each solid line represents the mean values of a sample of 20 simulation runs and the surrounding shaded regions visualise the sample standard deviation.

for practical application, the observational noise should not limit the quality of the results. Note that as this section aims to illustrate the intrinsic variability properties, the results are derived in the absence of observational noise. The latter requirement for the reference light curve becomes important in Sect. 3.4, where observational prospects are discussed.

Fig. 3.4 gives an example of the derived Fourier spectral-timing properties of the low-ionisation WA, plotted for one frequency bin, covering $(3.75-7.5)\times10^{-5}$ Hz. The power spectral density, intrinsic coherence, and time lags are plotted as a function of energy for six distances from the ionising source. Each of the displayed curves shows the mean value of the quantity determined from the twenty simulation runs, and the surrounding shaded regions represent the sample standard deviation to illustrate the spread between runs.

The timing properties exhibit a general robustness to the diverse light curves employed for the description of the continuum variability. As a result, it is, in principle, possible to discern the timing properties produced by gas of different conditions in each of the plotted

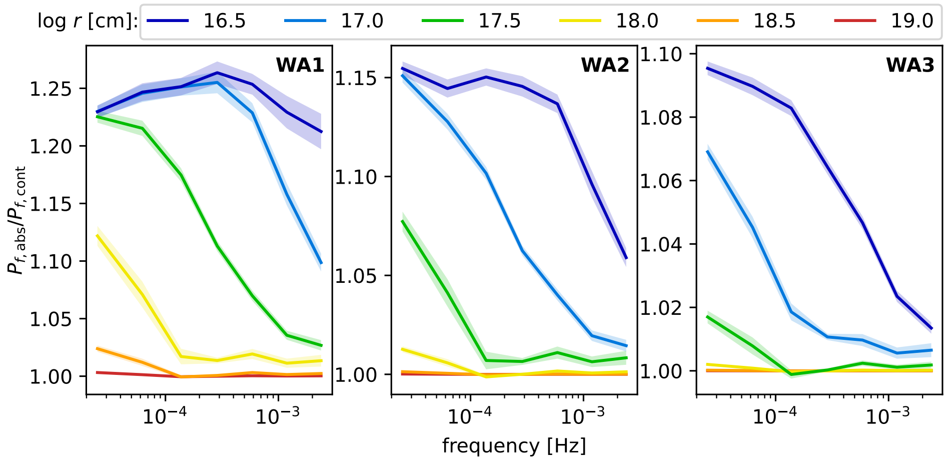

Figure 3.5: Power spectrum of the 0.6–1.1 keV band relative to an unabsorbed continuum light curve as a function of Fourier frequency. The absorption-affected energy band contains the most variable features in each simulated WA. The lines represent the mean values of this ratio, derived from the sample of 20 simulation runs, and the shaded areas symbolise the associated standard deviation. The power spectra from each simulation run were averaged over multiple frequencies using logarithmic binning with $\Delta \log f = 2$ before evaluating the ratio.

quantities. As expected, the unobserved history of the WA has the largest impact in the case of the most delayed response, which in the case of WA1 corresponds to 10^{18} cm (yellow curve in Fig. 3.4). This effect translates most visibly to the intrinsic coherence, where the scatter is significantly larger than in other scenarios. In contrast, the scatter in the power spectra is mostly intrinsic to the underlying variability process, i.e. it reflects the differences in the input light curves that were used for the simulations (Fig. 3.3). Moreover, it is correlated across different energy bands from the design of the simulations. The scatter due to the differences in each simulation dependent on the absorber response is significantly smaller (see Fig. 3.5 introduced in the text below).

The aspects of the spectral-timing properties related to the gas density (or distance from the ionising source) are discussed in detail below.

3.3.1 Timescale-dependent variability amplitude

The energy-resolved power spectrum in Fig. 3.4 is given for the second lowest probed frequency bin in our analysis, corresponding to 27–13 ks. At this timescale, the power spectrum of the smallest two distances given in the plot is indistinguishable. This behaviour results from the fact that the gas recombination timescale is significantly smaller, and thus the variability at low frequencies remains very high. Fig. 3.5 reveals how that changes with increasing frequency. The three panels show the ratio of the power spectrum measured in the energy range covering the most highly variable features of each outflow, relative to an

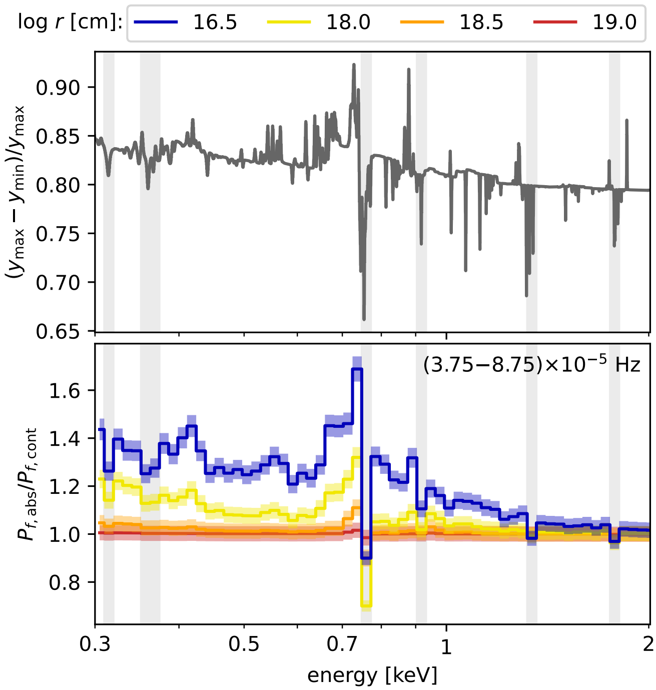

Figure 3.6: The effect of anti-correlated absorption signal in the energy-resolved power spectrum derived from simulations with the *Athena* X-IFU response. Top panel: relative difference of the highest- and lowest-flux spectrum in the simulation with a rapidly responding WA1 located at $10^{16.5}$ cm. Bottom panel: power spectrum vs. energy of WA1 at four distances normalised by the value of the power spectrum in an unabsorbed band. The energy bins where the power spectrum drops due to the anti-correlation of the continuum and absorption signal are highlighted. The feature at $\approx$0.75 keV is produced by the iron UTA.

absorption-free band. Essentially, the gas response acts as a low-pass filter, suppressing variability at high frequencies. As the probed frequency becomes comparable to and eventually exceeds the recombination timescale, the relative variability drops considerably. As the recombination rates are proportional to the gas density and thus inversely proportional to the distance given the same gas ionisation, this decrease occurs at lower frequencies for more distant outflows. The recombination timescale is also generally smaller for more highly ionised gas, which can be easily seen by comparing the behaviour between the three panels.

In the case of the outflows simulated here, an increase in the incident ionising flux is mostly followed by a rise in the absorber opacity in the soft X-ray band. The changes in the ionisation state of the gas however naturally produce also the opposite effect, visible in our data in several absorbed energy bins. As a result of this anti-correlation between the continuum and the absorption signal, the power spectrum in the affected energy bins can drop significantly relative to neighbouring bins, in some cases reaching below the continuum level.

In the simulations with energy resolution of EPIC-pn, this effect is mostly suppressed as the energy band used for the extraction of such light curves is contaminated by other absorption features with the opposite behaviour. In the bottom panel of Fig. 3.6, the power spectrum vs. energy is plotted for simulations done with the X-IFU response, which has significantly higher energy resolution. To further benefit from this improvement with respect to EPIC-pn, the examined energy range is divided into twice as many energy bins, which reveals these effects with even higher clarity. To draw a straightforward connection of the power-spectrum features to the corresponding (time-domain) flux in a given energy bin, we present the relative difference of the highest-flux spectrum to the lowest-flux spectrum of the effectively instantaneously responding gas ($r = 10^{16.5}$ cm) in the top panel of Fig. 3.6.

As the energy bin width allows nearby absorption lines from elements in different ionisation states to be separated, a typical behaviour can be observed in the data. Most notable in the plot is the iron UTA, around 0.75 keV. The power spectra in the affected bands capture how the lower ionisation states (with transitions mostly left-ward of the highlighted energy bin) become more populated with decreasing ionising flux, resulting in correlated variability and thus a peak in the power spectra. As fewer more-highly-ionised ions are available to absorb the incoming radiation (in the highlighted band) as a result, the associated absorption becomes weaker and thus anti-correlated with the continuum, effectively reducing the variability amplitude in the absorbed band.

3.3.2 Coherence and time lags

Fig. 3.7 extends the overview of the energy-dependent coherence and time lags to all three absorbers, simulated with the X-IFU energy resolution. The coherence spectra plotted in the top panels show that the outflows are generally highly coherent with the continuum, irrespective of their ability to respond to the ionising flux. With that, the time lags, defined for coherent signals, are related to real delays in the data. Nevertheless, the measured values cannot be directly interpreted as the delay in the absorber response. Particularly, the increasingly longer response time, growing with decreasing density (increasing distance), eventually suppresses the measured Fourier time lags due to decreasing variability amplitude (Uttley et al. 2014). As a result, especially when only one frequency bin is considered, lag-energy spectra of differently responding outflows may be difficult to discern (see e.g. the yellow and dark blue lines in the middle column of Fig. 3.7).

Additionally, the bottom panels reveal positive-sign lags in several energy bands, which can result from the anti-correlation of the absorber signal with the continuum. The frequency-domain complex polar representation of the analysed light curve pair allows for an intuitive explanation of this effect. With this approach, the Fourier transform at each frequency describes the signal with an amplitude and phase, where the phase difference between two signals translates into the time-lag (Uttley et al. 2014). The anti-correlation then introduces an additional phase shift of π, creating an artificial, opposite-sign time lag component. Note

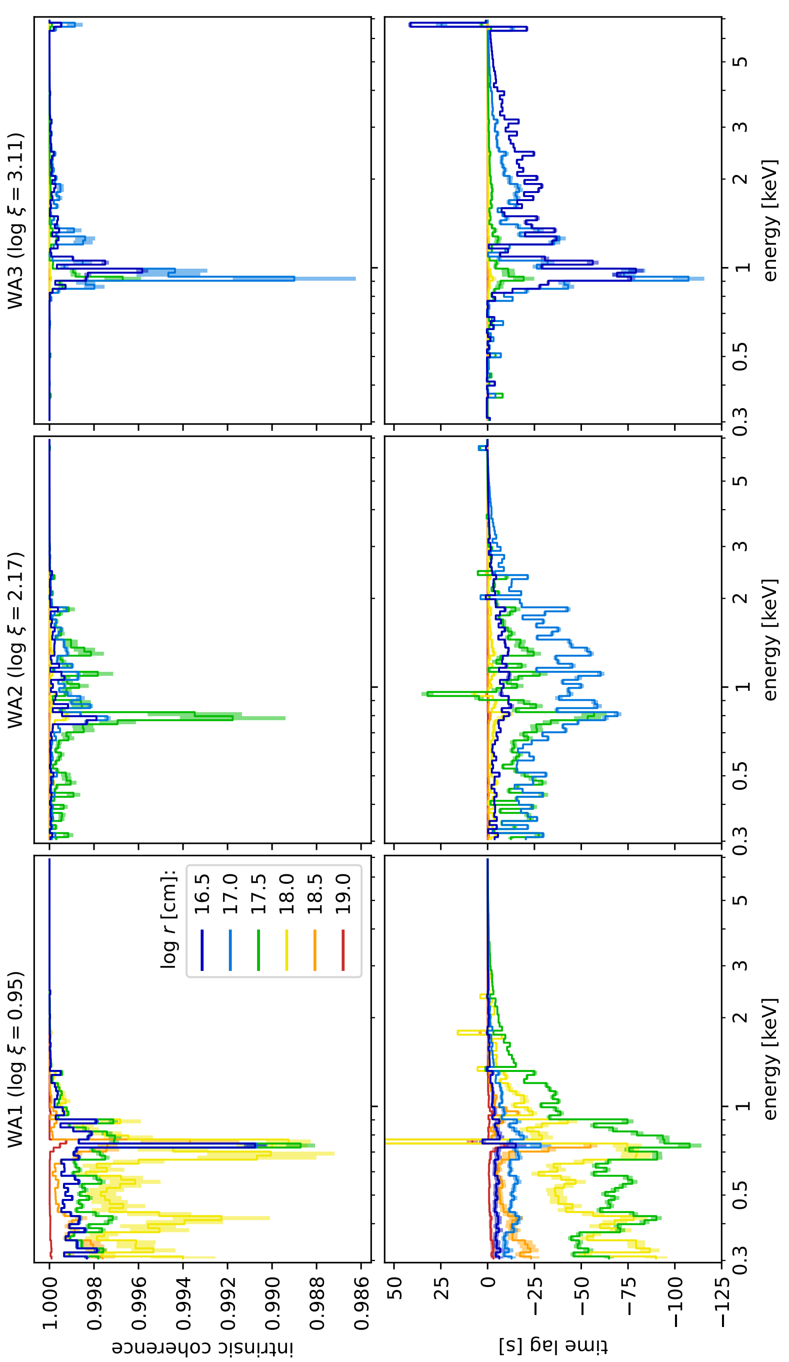

Figure 3.7: Intrinsic coherence (top row) and time lags (bottom row) of the three simulated outflows (columns) plotted as a function of energy. The results are plotted for the frequency range $(3.75-7.5)\times10^{-5}$ Hz.

that the energy bands with positive lags in the bottom left panel of Fig. 3.7 can be identified also in the energy-resolved power spectrum in Fig. 3.6, where the value drops below the continuum level.

3.4 Discussion

The conditions in the AGN–outflow systems simulated here probe a different regime than the UFO-like outflows investigated in Juráňová et al. (2022). The variability is intrinsically more coherent in all probed absorbers, regardless of the outflow response timescale. The qualitatively different behaviour is a consequence of two main factors: the variability amplitude of the continuum and the relative strength of the absorption signal. Regarding the former, the system simulated in (Juráňová et al. 2022) is based on an extremely variable NLS1, specifically IRAS 13224–3809. Its continuum varies on timescales of hours to days by a factor of ten, whereas in the source simulated here, the typical flux variations are about three times smaller. This influences the range of changes in the ionic concentrations and, consequently, the line optical depths reached by the absorbers.

The second reason arises from the fact that the coherence that is observed is the measure of linearity between the (reference) continuum and the product of the absorption variability with the continuum again, extracted from the band of interest. As a result, the intrinsic coherence of the absorption alone can be suppressed in the data by the high coherence of a strong underlying continuum. In the case of the absorbers modelled by Juráňová et al., the relative contribution of the absorption signal to the total variability is higher with respect to the conditions in the systems modelled here. Their absorbers have a larger column density, and the turbulent velocity broadening is assumed to be greater (1000 $\mathrm{km\,s^{-1}}$), reflecting conditions expected for ultra-fast outflows. This results in a substantially lower level of saturation, allowing greater variability of the absorption light curve (see Fig. 12 in Juráňová et al. 2022).

Interestingly, the coherence below $\sim$0.7 and above $\sim$1.5 keV in the 2001 observations of MCG–06-30-15 is significantly lower than one (Kara et al. 2014). This decrease, reported for the data that serve as a basis for our simulations, becomes even stronger in later observations, impacting the entire spectral range of EPIC-pn. While the authors explain these features with geometrical changes of the emission sources, the intrinsic absorption from ionised outflows could, in principle, also contribute to their existence. Moreover, (Igo et al. 2020) found signatures of variable outflows in this source by detecting isolated features in excess-variance spectra.

In this work, the WAs are simulated independently, and thus precise quantification of the possible contribution of the outflows to the decrease in coherence cannot be directly made. Nevertheless, based on the observed magnitude of the reported coherence drops and the affected spectral range, it is unlikely that outflows with a changing ionisation state provide a dominant contribution to the coherence spectrum pattern. It should be noted, however, that variability associated with the absorbing medium can originate also from the geometrical properties of the outflow. For example, variability uncorrelated with the ionising flux can

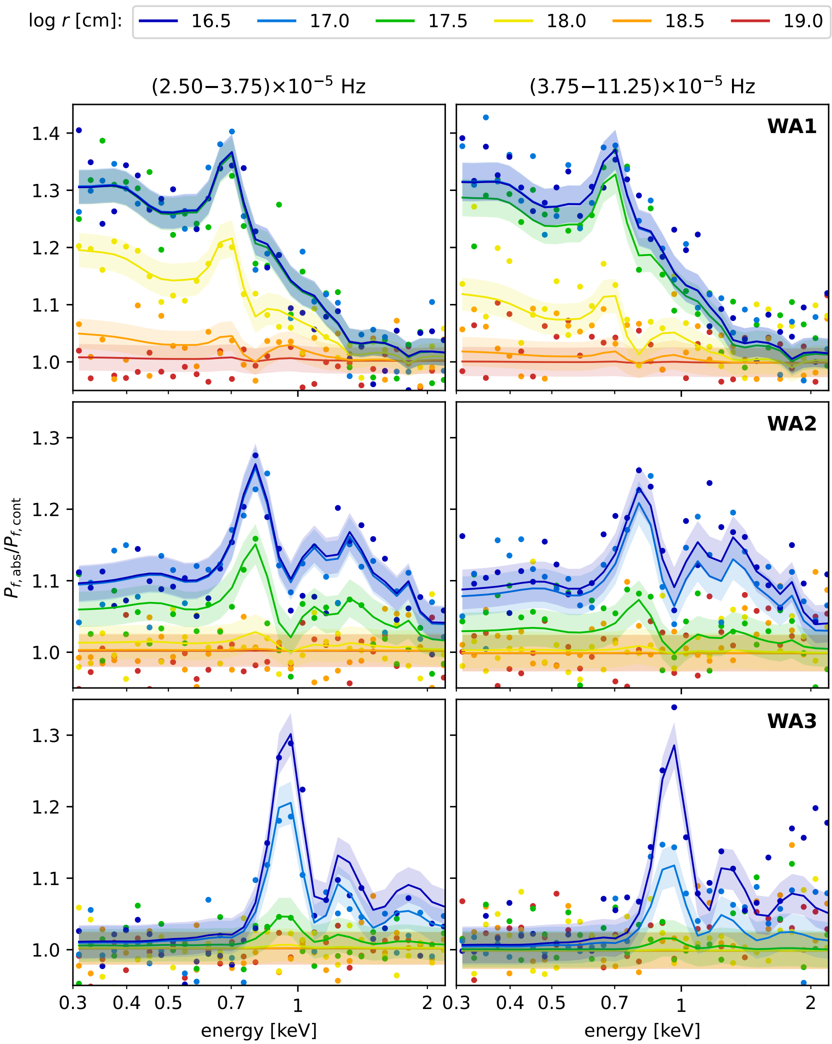

Figure 3.8: Example of the expected observability of the power spectrum vs. energy for the three simulated outflows (rows) in two frequency bins (columns), normalised by the power-spectrum of the unabsorbed continuum. Each solid line represents the mean values of a sample of 20 (observational-noise-free) simulation runs and the surrounding shaded regions visualise the sample standard deviation. The dots represent an example of the observed power spectrum from one of the runs, with Poisson noise applied to the analysed light curves to mimic observing conditions with EPIC-pn.

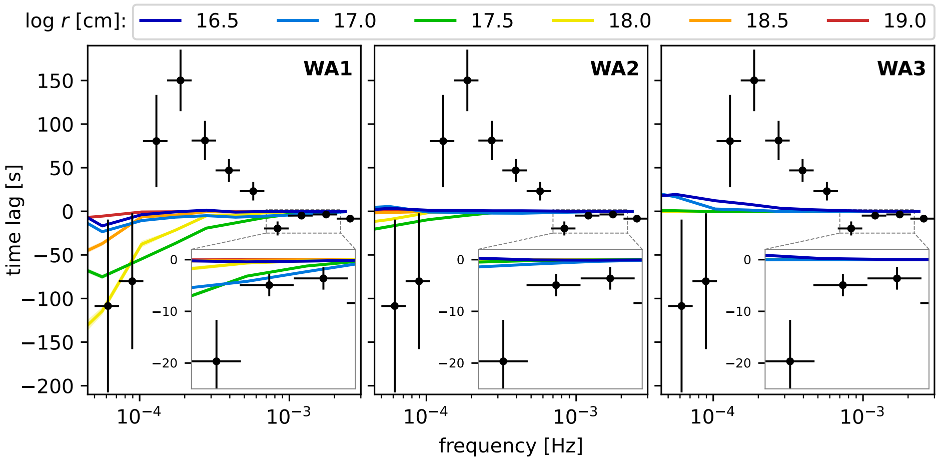

Figure 3.9: Broad-band lag-frequency spectra between 0.3−1 keV and 1−4 keV bands overlaid with time lags measured in MCG–06-30-15 between the same bands by Kara et al. (2016).

arise due to changes in the column density covering the compact source, if the gas is crossing the line of sight to the AGN core with sufficiently high transverse velocity (e.g. Costantini et al. 2007a; Matt et al. 2011; Longinotti et al. 2013). However, modelling such behaviour requires strong assumptions about the absorber structure which currently cannot be independently constrained.

In AGN X-ray studies, time lags are often used to investigate the relationship between different emission regions. However, as demonstrated by Silva et al. (2016), lags arising from the delayed response of absorbers can also be measurable. Nevertheless, when analysing broad-band light curves with high coherence, the observed lags are typically interpreted solely in terms of the underlying emission (reviewed e.g. by Cackett et al. 2021), neglecting the potential influence of intrinsic ionised absorbers present in the broad-band spectrum.

As the relation between the high-energy-resolution lag-energy spectra (Fig. 3.7) and broad-band lags is rather complex, we provide, for convenience, an illustration of the frequency-dependent lags between 0.3–1 keV and 1–4 keV light curves in Fig. 3.9, along with the lags measured in MCG–06-30-15 by Kara et al. (2016). As these energy bands do not take account of the location of the absorption features, the lags are significantly suppressed for WA2 and become positive for WA3 due to the shift of the bulk of the lines to the hard band. From the comparison with the observational constraints, it is apparent that these two higher-ionisation outflows may contribute to the observed lags only minimally, regardless of their distance from the emission source. In contrast, the largest (negative) lags from the low-ionisation WA are comparable to the lags measured below 10^{-4} Hz. However, the continuum lags at low frequencies, generally dominated by the (positive) lags from the inward propagation of accretion-disc fluctuations (Arévalo & Uttley 2006), likely contribute to the total observed lags as well. Considering that the relation between the individual components of the lagging signal and the measured lags is non-trivial, the low-frequency lags from delayed absorption from the low-ionisation absorber may indeed significantly affect the total observed lags.

At frequencies typical for the (negative) reverberation lag (Fabian et al. 2009; Zoghbi et al. 2010), above $\sim 3 \times 10^{-4}$ Hz, the predicted broad-band WA lags are on the order of $\lesssim 10$ s, and approach zero at even shorter timescales. In MCG–06-30-15, the putative reverberation lag is detected only above 7×10^{-4} Hz, where the absorber lags are negligible for all except two scenarios tested for WA1. Nonetheless, also in these two cases, $r = 10^{17}$ and $10^{17.5}$ cm, the WA lags are by a factor of four smaller than the largest value of the observed negative lag.

Disentangling absorption-related lags from other spectral components with present-day data is a complicated task due to the inherent complexity of the sources and requirements on the signal-to-noise ratio. In contrast, Fig. 3.8 shows that the power spectra can be retrieved with high enough precision and energy resolution to identify outflows present at different distances. The two columns show the simulated energy-dependent power spectra for two adjacent frequency bins, with each WA in a different row. The data points correspond to the power spectra obtained from the simulated observations with observational (Poisson) noise applied. The modelled power spectrum free of this noise contribution is given as in Fig. 3.4, with a solid line and the surrounding shaded area, including the scatter due to the fundamentally unobservable true variability of the AGN emission. Given the intrinsically narrow appearance of these features in the energy-resolved power spectra, it may be possible to use this approach to isolate the outflow signature and place constraints on its location and density.

3.5 Summary

In this paper, we probe the spectral-timing properties of ionised outflows in a highly variable AGN, and examine their sensitivity to the intrinsic variability of the background, ionising source akin to MCG–06-30-15. We do so by simulating synthetic observations with high temporal resolution of spectra featuring warm absorbers of different physical properties. The simulated data are based on an observing campaign with *XMM-Newton* consisting of three observations separated by ~ 50 ks gaps. The Fourier spectral timing analysis yielded the following major findings.

1. The unknown history of the system does not significantly impact the absorber timing properties recovered from the observed periods, regardless of the time required for the absorbing medium to respond to changes in the incident ionising radiation.
2. Concerning the intrinsic coherence between the continuum-emission and absorption signal, the simulations probe a different, highly coherent, regime of the absorber response relative to the system presented in Juráňová et al. (2022).
3. If present in the data, the variable absorption signal can be inadvertently detected in broad-band time lags in currently available observations from *XMM-Newton*. Depending on the gas response, present ions and the analysed energy bands, the magnitude of

these lags can exceed $\sim$100 s below 10^{-4} Hz, and generally decrease with increasing frequency.

4. Depending on the gas density (or distance to the ionising source), the absorber variability and the presence of contaminating time lags can be revealed with the energy-resolved power spectra of absorption-affected spectral bands.
5. If modelled with the observed variability of the underlying continuum, energy-resolved power spectra can be used to place constraints on the density and consequently the distance of ionised outflows in *XMM-Newton* EPIC-pn data.